

Depth-resolved measurements with elliptically polarized reflectance spectroscopy

MARIA J. BAILEY^{1,2} AND KONSTANTIN SOKOLOV^{1,2,3,*}

¹Department of Imaging Physics, MD Anderson Cancer Center, Houston, TX 77030, USA

²Department of Biomedical Engineering, University of Texas at Austin, Austin, TX 78712, USA

³Department of Bioengineering, Rice University, Houston, TX 77005, USA

*ksokolov@mdanderson.org

Abstract: The ability of elliptical polarized reflectance spectroscopy (EPRS) to detect spectroscopic alterations in tissue mimicking phantoms and in biological tissue in situ is demonstrated. It is shown that there is a linear relationship between light penetration depth and ellipticity. This dependence is used to demonstrate the feasibility of a depth-resolved spectroscopic imaging using EPRS. The advantages and drawbacks of EPRS in evaluation of biological tissue are analyzed and discussed.

©2016 Optical Society of America

OCIS codes: (290.5855) Scattering, polarization; (170.6510) Spectroscopy, tissue diagnostics; (290.0290) Scattering; (300.0300) Spectroscopy

References and links

1. J. Q. Brown, K. Vishwanath, G. M. Palmer, and N. Ramanujam, "Advances in quantitative UV-visible spectroscopy for clinical and pre-clinical application in cancer," *Curr. Opin. Biotechnol.* **20**(1), 119–131 (2009).
2. R. Richards-Kortum and E. Sevick-Muraca, "Quantitative optical spectroscopy for tissue diagnosis," *Annu. Rev. Phys. Chem.* **47**(1), 555–606 (1996).
3. I. J. Bigio and J. R. Mourant, "Ultraviolet and visible spectroscopies for tissue diagnostics: fluorescence spectroscopy and elastic-scattering spectroscopy," *Phys. Med. Biol.* **42**(5), 803–814 (1997).
4. L. Qiu, V. Turzhitsky, R. Chuttani, D. Pleskow, J. D. Goldsmith, L. Guo, E. Vitkin, I. Itzkan, E. B. Hanlon, and L. T. Perelman, "Spectral imaging with scattered light: from early cancer detection to cell biology," *IEEE J. Sel. Top. Quantum Electron.* **18**(3), 1073–1083 (2012).
5. T. E. Matthews, M. Medina, J. R. Maher, H. Levinson, W. J. Brown, and A. Wax, "Deep tissue imaging using spectroscopic analysis of multiply scattered light," *Optica* **1**(2), 105–111 (2014).
6. Y. Zhu, N. G. Terry, and A. Wax, "Angle-resolved low-coherence interferometry: an optical biopsy technique for clinical detection of dysplasia in Barrett's esophagus," *Expert Rev. Gastroenterol. Hepatol.* **6**(1), 37–41 (2012).
7. L. T. Nieman, C.-W. Kan, A. Gillenwater, M. K. Markey, and K. Sokolov, "Probing local tissue changes in the oral cavity for early detection of cancer using oblique polarized reflectance spectroscopy: a pilot clinical trial," *J. Biomed. Opt.* **13**(2), 024011 (2008).
8. I. Pavlova, K. Sokolov, R. Drezeck, A. Malpica, M. Follen, and R. Richards-Kortum, "Microanatomical and biochemical origins of normal and precancerous cervical autofluorescence using laser-scanning fluorescence confocal microscopy," *Photochem. Photobiol.* **77**(5), 550–555 (2003).
9. K. Sokolov, M. Follen, and R. Richards-Kortum, "Optical spectroscopy for detection of neoplasia," *Curr. Opin. Chem. Biol.* **6**(5), 651–658 (2002).
10. B. C. Wilson, E. M. Sevick, M. S. Patterson, and B. Chance, "Time-dependent optical spectroscopy and imaging for biomedical applications," *Proc. IEEE* **80**(6), 918–930 (1992).
11. B. B. Das, K. M. Yoo, and R. R. Alfano, "Ultrafast time-gated imaging in thick tissues: a step toward optical mammography," *Opt. Lett.* **18**(13), 1092–1094 (1993).
12. G. Mitic, J. Kölzer, J. Otto, E. Plies, G. Sölkner, and W. Zinth, "Time-gated transillumination of biological tissues and tissuelike phantoms," *Appl. Opt.* **33**(28), 6699–6710 (1994).
13. K. Sokolov, R. Drezeck, K. Gossage, and R. Richards-Kortum, "Reflectance spectroscopy with polarized light: is it sensitive to cellular and nuclear morphology," *Opt. Express* **5**(13), 302–317 (1999).
14. V. Backman, R. Gurjar, K. Badizadegan, I. Itzkan, R. R. Dasari, L. T. Perelman, and M. S. Feld, "Polarized light scattering spectroscopy for quantitative measurement of epithelial cellular structures in situ," *IEEE J. Sel. Top. Quantum Electron.* **5**(4), 1019–1026 (1999).
15. R. R. Anderson, "Polarized light examination and photography of the skin," *Arch. Dermatol.* **127**(7), 1000–1005 (1991).
16. S. L. Jacques, J. R. Roman, and K. Lee, "Imaging superficial tissues with polarized light," *Lasers Surg. Med.* **26**(2), 119–129 (2000).

17. Y. Liu, Y. Kim, X. Li, and V. Backman, "Investigation of depth selectivity of polarization gating for tissue characterization," *Opt. Express* **13**(2), 601–611 (2005).
18. S. G. Demos and R. R. Alfano, "Temporal gating in highly scattering media by the degree of optical polarization," *Opt. Lett.* **21**(2), 161–163 (1996).
19. S. Morgan and M. Ridgway, "Polarization properties of light backscattered from a two layer scattering medium," *Opt. Express* **7**(12), 395–402 (2000).
20. D. Roblyer, R. Richards-Kortum, K. Sokolov, A. K. El-Naggar, M. D. Williams, C. Kurachi, and A. M. Gillenwater, "Multispectral optical imaging device for in vivo detection of oral neoplasia," *J. Biomed. Opt.* **13**, 024019 (2008).
21. L. Qiu, D. K. Pleskow, R. Chuttani, E. Vitkin, J. Leyden, N. Ozden, S. Itani, L. Guo, A. Sacks, J. D. Goldsmith, M. D. Modell, E. B. Hanlon, I. Itzkan, and L. T. Perelman, "Multispectral scanning during endoscopy guides biopsy of dysplasia in Barrett's esophagus," *Nat. Med.* **16**(5), 603–606 (2010).
22. C. M. Macdonald, S. L. Jacques, and I. V. Meglinski, "Circular polarization memory in polydisperse scattering media," *Phys. Rev. E Stat. Nonlin. Soft Matter Phys.* **91**(3), 033204 (2015).
23. S. Rehn, A. Planat-Chrétien, M. Berger, J.-M. Dinten, C. Deumié, and A. da Silva, "Depth probing of diffuse tissues controlled with elliptically polarized light," *J. Biomed. Opt.* **18**(1), 016007 (2013).
24. R. A. Schwarz, D. Arifler, S. K. Chang, I. Pavlova, I. A. Hussain, V. Mack, B. Knight, R. Richards-Kortum, and A. M. Gillenwater, "Ball lens coupled fiber-optic probe for depth-resolved spectroscopy of epithelial tissue," *Opt. Lett.* **30**(10), 1159–1161 (2005).
25. O. R. Šćepanović, Z. Volynskaya, C. R. Kong, L. H. Galindo, R. R. Dasari, and M. S. Feld, "A multimodal spectroscopy system for real-time disease diagnosis," *Rev. Sci. Instrum.* **80**(4), 043103 (2009).
26. R. A. Schwarz, W. Gao, C. Redden Weber, C. Kurachi, J. J. Lee, A. K. El-Naggar, R. Richards-Kortum, and A. M. Gillenwater, "Noninvasive evaluation of oral lesions using depth-sensitive optical spectroscopy," *Cancer* **115**(8), 1669–1679 (2009).
27. A. Amelink, H. J. C. M. Sterenborg, M. P. L. Bard, and S. A. Burgers, "In vivo measurement of the local optical properties of tissue by use of differential path-length spectroscopy," *Opt. Lett.* **29**(10), 1087–1089 (2004).
28. L. Nieman, A. Myakov, J. Aaron, and K. Sokolov, "Optical sectioning using a fiber probe with an angled illumination-collection geometry: evaluation in engineered tissue phantoms," *Appl. Opt.* **43**(6), 1308–1319 (2004).
29. A. M. J. Wang, J. E. Bender, J. Pfeifer, U. Utzinger, and R. A. Drezek, "Depth-sensitive reflectance measurements using obliquely oriented fiber probes," *J. Biomed. Opt.* **10**(4), 044017 (2005).
30. D. Arifler, R. A. Schwarz, S. K. Chang, and R. Richards-Kortum, "Reflectance spectroscopy for diagnosis of epithelial precancer: model-based analysis of fiber-optic probe designs to resolve spectral information from epithelium and stroma," *Appl. Opt.* **44**(20), 4291–4305 (2005).
31. R. Reif, O. A' Amar, and I. J. Bigio, "Analytical model of light reflectance for extraction of the optical properties in small volumes of turbid media," *Appl. Opt.* **46**(29), 7317–7328 (2007).
32. A. Garcia-Urbe, N. Kheirnavaz, G. Marquez, V. Prieto, M. Duvic, and L. V. Wang, "Skin cancer detection by spectroscopic oblique-incidence reflectometry: classification and physiological origins," *Appl. Opt.* **43**(13), 2643–2650 (2004).
33. L. T. Nieman, M. Jakovljevic, and K. Sokolov, "Compact beveled fiber optic probe design for enhanced depth discrimination in epithelial tissues," *Opt. Express* **17**(4), 2780–2796 (2009).
34. F. C. MacKintosh, J. X. Zhu, D. J. Pine, and D. A. Weitz, "Polarization memory of multiply scattered light," *Phys. Rev. B Condens. Matter* **40**(13), 9342–9345 (1989).
35. Y. L. Kim, P. Pradhan, M. H. Kim, and V. Backman, "Circular polarization memory effect in low-coherence enhanced backscattering of light," *Opt. Lett.* **31**(18), 2744–2746 (2006).
36. I. M. Stockford, S. P. Morgan, P. C. Chang, and J. G. Walker, "Analysis of the spatial distribution of polarized light backscattered from layered scattering media," *J. Biomed. Opt.* **7**(3), 313–320 (2002).
37. A. Da Silva, C. Deumié, and I. Vanzetta, "Elliptically polarized light for depth resolved optical imaging," *Biomed. Opt. Express* **3**(11), 2907–2915 (2012).
38. R. Ahuja, J. Osorio-Guillen, J. S. de Almeida, B. Holm, W. Ching, and B. Johansson, "Electronic and optical properties of γ -Al₂O₃ from ab initio theory," *J. Phys. Condens. Matter* **16**(16), 2891–2900 (2004).
39. I. Seo, C. K. Hayakawa, and V. Venugopalan, "Radiative transport in the delta-P1 approximation for semi-infinite turbid media," *Med. Phys.* **35**(2), 681–693 (2008).
40. B. W. Pogue, and M. S. Patterson, "Review of tissue simulating phantoms for optical spectroscopy, imaging and dosimetry," *J. Biomed. Opt.* **11**, 041102 (2006).
41. C. Maetzler, <http://omlc.org/software/mie/maetzlermie/mie.m2013>.
42. C. F. Bohren and D. R. Huffman, *Absorption and Scattering of Light by Small Particles* (John Wiley & Sons, 2008).
43. J. M. Schmitt and G. Kumar, "Optical scattering properties of soft tissue: a discrete particle model," *Appl. Opt.* **37**(13), 2788–2797 (1998).
44. S. Prahl, <http://omlc.org/software/iad/2013>.
45. S. L. Jacques, "Optical properties of biological tissues: a review," *Phys. Med. Biol.* **58**(11), R37–R61 (2013).
46. Y. L. Kim, Y. Liu, R. K. Wali, H. K. Roy, M. J. Goldberg, A. K. Kromin, K. Chen, and V. Backman, "Simultaneous measurement of angular and spectral properties of light scattering for characterization of tissue

- microarchitecture and its alteration in early precancer,” *IEEE J. Sel. Top. Quantum Electron.* **9**(2), 243–256 (2003).
47. F. Ayers, A. Grant, D. Kuo, D. J. Cuccia, and A. J. Durkin, “Fabrication and characterization of silicone-based tissue phantoms with tunable optical properties in the visible and near infrared domain,” in *Biomedical Optics (BiOS) 2008* (International Society for Optics and Photonics, 2008), pp. 687007–687007–687009.
 48. Y. Zhang, B. Chen, and D. Li, “Propagation of polarized light in the biological tissue: a numerical study by polarized geometric Monte Carlo method,” *Appl. Opt.* **55**(10), 2681–2691 (2016).
 49. S. Bloom and H. Margenau, “Quantum theory of spectral line broadening,” *Phys. Rev.* **90**(5), 791–794 (1953).
 50. T. Fabritius, S. Makita, Y. Hong, R. Myllylä, and Y. Yasuno, “Automated retinal shadow compensation of optical coherence tomography images,” *J. Biomed. Opt.* **14**, 010503 (2009).
 51. E. J. Seibel and Q. Y. Smithwick, “Unique features of optical scanning, single fiber endoscopy,” *Lasers Surg. Med.* **30**(3), 177–183 (2002).
 52. S. J. Miller, C. M. Lee, B. P. Joshi, E. J. Seibel, and T. D. Wang, “In vivo multi-spectral wide-field fluorescence detection of dysplasia in the mouse,” *Gastroenterology* **140**, S11 (2011).

1. Introduction

Quantitative optical spectroscopic methods have shown immense potential in noninvasively extracting information from biological tissues [1–6]. Identifying correlations between tissue scattering and absorption spectra and tissue anatomical structures can lead to new non-invasive approaches for earlier detection and monitoring of various pathologies including cancer and cardiovascular diseases. Because biological tissue anatomy often consists of multilayer structures, alterations in tissue scattering and absorption properties are depth-dependent. Some pathological conditions such as neoplastic changes in the epithelial tissue and the underlying stroma are associated with concurrent changes in optical tissue properties at different depths [7–9]. Therefore, the ability to extract these optical signatures from several depths simultaneously is crucial from a clinical perspective. In reflectance spectroscopy, several methods have been implemented in order to achieve depth-resolved measurements. For example, time gating can separate photons based on their optical pathlengths, however, this approach requires highly sophisticated and expensive equipment [10–12]. In an alternative method, our group and others have developed a simple linear polarization gating to isolate tissue signals originating from shallow depths in tissues from the diffuse background of the underlying stroma using spectroscopic and imaging setups [13–21]. In polarization gated spectroscopy and imaging, polarized photons maintain their incident polarization for a particular number of mean free paths (MFP) depending on density of optical scatterers and their properties such as anisotropy factor [22, 23]. In linear polarization gating, a sample is illuminated with a linear polarized light and two components of the scattered light are detected: the co-polarized signal with its polarizations parallel to the incident polarization (I_{\parallel}) and the cross-polarized signal with its polarization orthogonal to the incident light (I_{\perp}). The I_{\parallel} signal is comprised of singly scattered photons originating from shallow depths in tissue along with multiply scattered photons that traveled deeper into the sample. In contrast, the I_{\perp} signal is dominated by multiply scattered photons. Subtracting the cross-linear polarized component from the co-linear polarized signal results in a linear polarization gated signal ($\Delta I = I_{\parallel} - I_{\perp}$) that consists predominantly of light scattered from shallow depths.

Therefore, linear polarization gating allows discrimination of single scattered photons from multiply scattered photons, but the selective detection of scattered signal from specific depths or layers within tissue remains a challenge. Recently, a number of approaches have been proposed to address this challenge including the use of spherical lenses [24–26], differential path length spectroscopy [27], or the use of fibers in an oblique orientation in order to favorably collect either superficial or deep penetrating photons from predetermined depths [28–33]. A major shortcoming of these systems is that they require multiple fibers with different fibers collecting signals from various depths. While still fairly low cost, these designs usually require a fine alignment of multiple fibers and other optical elements that reduces overall robustness and reproducibility of the corresponding systems.

An ideal approach to depth-resolved reflectance spectroscopy would require signal collection from various depths within tissue using the same optical path. Here, we explore the

feasibility of such system that is based on the property of circular polarized light to maintain its polarization in highly scattering media at larger depths as compared to linearly polarized light due to the so called circular “polarization memory” effect [34, 35]. Circularly polarized light undergoes small-angle, forward scattering events in diffusely scattering media with Mie scatterers that are characterized by a predominately forward scattering phase function that largely preserves helicity for long distances in a turbid medium [22, 34, 36]. Furthermore, it was recently demonstrated that elliptically polarized light can be used to image scattering phantoms and biological tissue at different depths by varying the degree of ellipticity from linear to circular polarization [37]. In this study, we extend this concept to depth-resolved spectroscopic measurements using varying degree of ellipticity of excitation light. We demonstrate feasibility of acquiring depth-resolved reflectance spectra through a single collection channel using elliptical polarized reflectance spectroscopy (EPRS) in tissue-mimicking optical phantoms with dyes and biological absorbers. We also showed that EPRS can be extended to a depth-resolved spectroscopic imaging.

2. Methods

2.1 Polarization gating

The depth penetration of the detected photons depends on the polarization of the incident and backscattered light. The illumination and detection polarizations are listed in Table 1. I_{\parallel} and I_{\perp} signify co- and cross-linear polarizations, respectively, while I_{SS} denotes singly scattered photons and I_{MS} represents multiple scattered photons. Multiple scattered light contributes to scattering signals that are detected by both the co-linear and co-elliptical detection schemes. The contribution of the I_{MS} to each signal can be determined from the cross-linear polarized detection as was described in [13–15]. In linear polarization gating techniques, cross-linear signals are subtracted from co-linear signals to yield superficial, singly scattered photons that have maintained the incident polarization. EPRS follows this approach by subtracting cross-linear polarization signals from co-elliptical signals to amplify detection of photons scattered from intermediate depths. This method assumes that the amount of multiply scattered photons is the same for the linearly and elliptically polarized light. This assumption was previously evaluated using Monte Carlo simulations and it was determined that cross-linear polarized light is a good approximation for multiple-scattered circular polarized illumination [36].

Table 1. Illumination and detection schemes of experimental setup

Illumination	Detection	Category of photons
Linear	Co-linear	Singly scattered & multiply scattered light $I_{\parallel} = I_{SS,linear} + I_{MS}$
Linear	Cross-linear	Multiply scattered $I_{\perp} = I_{MS}$
Elliptical	Co-elliptical	Singly scattered & multiply scattered light $I_{co-elliptical} = I_{SS,elliptical} + I_{MS}$

2.2 Experimental system

The experimental setup used is shown in Fig. 1. The EPRS system was based on an upright Leica DM600 optical microscope equipped with a PARISS spectral imager (Lightform Inc.). Incident light from an external halogen light source (Dolan-Jenner Industries) was coupled into a 600 μm core diameter fused silica optical fiber (NA 0.22, Fiberguide Industries), collimated and then passed through a linear polarizer and achromatic quarter wave plate (Thorlabs, AQWP05M-600). The polarized light was delivered at an angle of 45° relative to

the collection arm, which was perpendicular to the sample. Backscattered photons from the samples were collected by a 4x microscope objective with a numerical aperture of 0.14 (No. 11581049, Leica). The collected light passed through a quarter wave plate (Thorlabs, AQWP05M-600) and an analyzer in the collection arm before being delivered to the prism-based PARRISS spectroscopic imaging system equipped with a planar array CCD detector (Pixis 400, Princeton instruments).

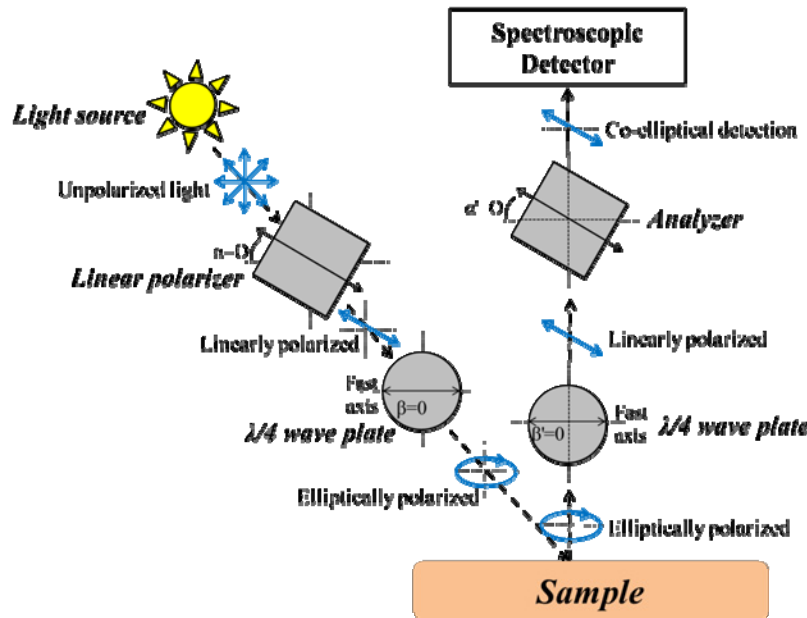


Fig. 1. Experimental setup of elliptical polarized reflectance spectroscopy system. Angle of incidence of the illumination was 45° relative to the sample surface. The rotation angles of the linear polarizers and quarter-wave plates are indicated by α and β , respectively.

Depending on the relative rotation angle between the linear polarizer and quarter wave plate, illumination polarization was tuned to desired polarization states. When axis of the polarizer and quarter wave plate were aligned ($\alpha = \beta = 0^\circ$), linear polarization was obtained. An elliptical polarization was obtained when the fast axis of the quarter wave plate was oriented at angle θ relative to the axis of the linear polarizer; circular polarization corresponded to $\theta = 45^\circ$. To obtain co-linear and co-elliptical polarization, the angle between the secondary quarter wave plate and analyzer was adjusted so that the detection polarization was matched to that of the illumination light. Cross-polarized light was acquired when the angle θ of the analyzer was 90° relative to the quarter wave plate fast axis.

2.3 Scattering phantoms

Scattering phantoms were prepared using silicone, specifically polydimethylsiloxane (PDMS) (P-4, Eager Plastics), as its long shelf life and solid, yet flexible, composition makes it appealing as a base material. Also, the refractive index of PDMS is 1.43 that closely approximates tissue. Scattering was introduced using aluminum oxide (Al_2O_3 , $n = 1.77$ [38]) particles (Al-600, Atlantic Equipment Engineers) because they have an anisotropy coefficient (g) similar of biological tissue as discussed below [39, 40]. Moreover, the size distributions of the Al_2O_3 particles were confirmed to be in the Mie scattering regime. The size distributions of the Al_2O_3 particles were analyzed using dynamic light scattering (DelsaNano, Beckman Coulter). Using these size distribution ($1.04 \pm 0.818 \mu\text{m}$) in a modified version of Christian Maetzler's free source Mie code [41], based on the appendix in Bohren and Huffman [42], the

anisotropy coefficient of the Al_2O_3 particles was determined to be 0.89, 0.88, and 0.87 for 500 nm, 600 nm, and 700 nm, respectively. The Mie algorithm was revised such that the volume fractions according to the size distribution of the particles were accounted for in the calculation of optical scattering [43]. The concentration of Al_2O_3 required to simulate the desired reduced scattering coefficient was confirmed with Scott Prahl's widely-used Inverse Adding-Double Technique [44]. In these studies, we made phantoms mimicking breast tissue scattering with a reported reduced scattering coefficient of 1.3 mm^{-1} at 600 nm [45] using a concentration of 6.5 mg/mL Al_2O_3 in PDMS. The reduced scattering coefficient for this concentration of Al_2O_3 in PDMS changes from 1.4 mm^{-1} at 500 nm to 1.2 mm^{-1} at 700 nm. These changes in the scattering coefficient were considered negligible in our data analyses.

2.3.1 Single-layer model to examine depth penetration

To examine the depth penetration as a function of ellipticity, we adapted a method developed by Backman et al. to study the depth penetration of linear polarization gating [14, 46]. We varied the physical thickness of a phantom with Al_2O_3 in PDMS simulating breast tissue scattering. The scattering media of varying thicknesses was placed on top of a 10 mm thick non-scattering, transparent PDMS layer to minimize contributions from refractive index mismatch at the boundary of the scattering sample under study. Mineral oil ($n = 1.47$) was deposited between the layers, and any air bubbles were removed. The dimensions of the single-layer model along the x- and y-directions were $5 \text{ cm} \times 5 \text{ cm}$. Light scattering spectra were measured for each thickness. Integrated reflectance intensity in the 500-750 nm region was plotted as a function of thickness of the scattering phantoms to quantify the penetration depth of EPRS.

2.3.2 Multilayer phantoms to demonstrate depth-resolved spectroscopy

To further evaluate the depth sensitivity of EPRS, we used multilayer PDMS phantoms with embedded dyes. Dyes were incorporated into specific layers of the phantom in order to provide spectroscopic changes that could be detected as a function of depth. Initially, green and red food coloring (Model No. 054189 Great Value, Inc.) were used as the dyes under study as they have distinctly different absorption spectra (Fig. 2(a)) and are safe to handle. A concentration of 0.123 mg/mL for the green food coloring and 0.147 mg/mL of the red food coloring in PDMS produced a μ_a of 0.05 mm^{-1} at 540 nm. The absorbance of the dye layers was chosen to ensure sufficient perturbation of reflectance spectra for easy detection of the dyed layers while avoiding strong signal attenuation.

The procedure to produce robust, multilayer PDMS phantoms was adapted from Ayers et al. [47]. To ensure even distribution, 130 mg of scattering Al_2O_3 particles were added into 1.912 g of a curing agent (P-Series curing agent, Eager Plastics), mixed with a Vortex shaker, and then placed in an ultrasonic bath (Branson 1510R-MT) for 30 minutes. To prevent the Al_2O_3 particles from settling, the suspension was agitated with a Vortex shaker several times during this period. While the Al_2O_3 in curing agent suspension was in the ultrasonic bath, 20 mL (19.12 g by weight) of PDMS was mixed with either green (0.123 mg/mL concentration) or red (0.147 mg/mL) food coloring dye using a pipette. Then, the PDMS with or without dye and the Al_2O_3 /curing agent suspension were thoroughly mixed together in a 1 to 1 volume ratio for 15 minutes to begin the curing process. Different layers were produced in separate disposable petri dishes and were and placed into a vacuum desiccator for 20 minutes to draw out gasses produced during the curing process. The majority of the produced bubbles were popped through rapid depressurization of the vacuum desiccator. Any remaining air bubbles were manually punctured with a needle. Finally, plastic lids were placed over phantoms to prevent accumulation of dust and were allowed to cure at room temperature for 24 hours. Multilayer phantoms were constructed by stacking the prepared layers of PDMS with desired optical properties. The dimensions of the multi-layer model along the x- and y-directions were

5 cm \times 5 cm. Mineral oil was used as a matching fluid between each PDMS layer to avoid refractive index mismatches.

2.3.3 Vascular phantom

Heparinized whole bovine blood was used to demonstrate the ability of EPRS to observe depth-resolved spectroscopic changes associated with endogenous biological absorbers. To this end, a scattering PDMS phantom with a 500 μ m microchannel to flow blood through was engineered. First, a 3.5 mm thick scattering PDMS phantom was prepared in a petri dish. A metal 500 μ m diameter rod was placed on top of the phantom layer. Then, a mixture of Al_2O_3 particles in the curing solution and PDMS mixture was poured over the rod, degassed, and allowed to cure. The cured phantom was washed with acetone to invoke swelling and expansion of PDMS surrounding the rod. Then, the rod was carefully removed using pliers resulting in a phantom with a bottom 3.5 mm and a top 2 mm with a 500 μ m channel between the two layers (Fig. 7(a)). The dimensions of the vascular phantom along the x- and y-directions were 5 cm \times 5 cm. The microchannel was filled with heparinized bovine blood using two syringes attached to the input and output ports of the channel. The blood absorbance spectrum is shown in Fig. 2(b). The bovine blood was frozen and thawed for use, which accounts for the absorption peak at 630 nm associated with metmyoglobin due to oxidation.

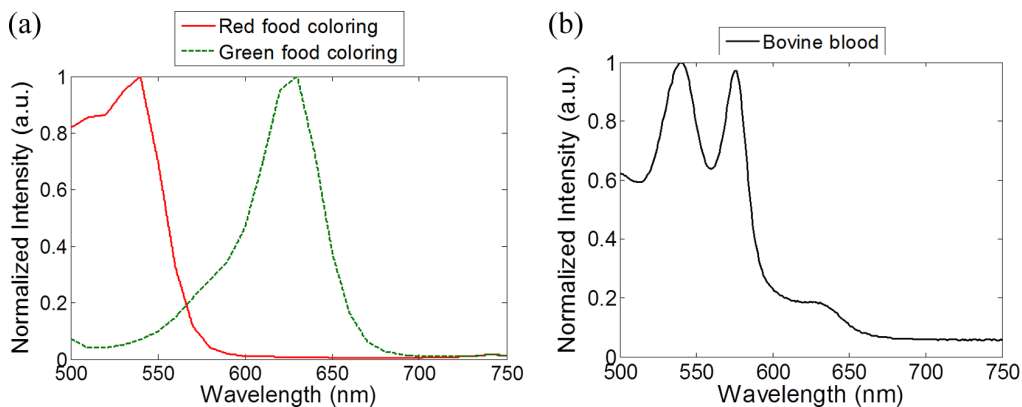


Fig. 2. Normalized absorbance spectra of (a) red and green food coloring and (b) bovine blood.

2.3.4 Murine measurements

An ear of an adult male nude mouse cadaver was used to measure blood microvessels in an animal within 10 minutes of the mouse being sacrificed. The ear was carefully flattened on a 10 mm slab of transparent PDMS and an index matching fluid ($n = 1.5$) was applied on the top to reduce surface reflections. Then, EPRS measurements were carried out in different locations on the ear. In each location the PARISS spectral imager acquired a spatially resolved line scan. Groups of twenty neighboring pixels were averaged along the line scan for each ellipticity to produce depth-resolved EPRS spectra at each spatial location (1 pixel = 6.25 μ m). These data were presented as a depth-resolved two-dimensional image of blood distribution. The relative amount of blood was estimated by subtracting the integrated intensity of 600-640 nm spectral region from the intensity of the 530-570 nm region which correspond to low and high hemoglobin absorbance, respectively.

2.4 Data analysis

For each sample, scattered light was measured with polarization co-linear, cross-linear, and co-elliptical (5° to 45° at intervals of 5°) relative to the illumination light polarization. Polarization gated spectra were obtained by subtracting the cross-linear signal from the co-

linear and co-elliptical signals. The obtained raw spectra were normalized using a diffuse reflectance substrate standard (SRS-99, Labsphere, Inc.) to account for the spectral responses of the source and detector. Additionally, the signals were also normalized by the exposure time.

To quantify absorbance in depth-dependent reflectance measurements of multilayer phantoms, we prepared pairs of tissue phantoms with matching scattering properties and geometries with and without embedded chromophores. Reflectance spectra of the phantoms with dyes were subtracted from the ones with no dye. This approach allowed us to remove scattering background and to convert absorption dips in reflectance spectra into positive peaks for quantitative analyses of the spectra. Then, spectral regions corresponding to absorption of chromophores were integrated and were corrected for any DC offsets by subtracting an integrated intensity value of regions with minimum dye absorption. The integrated wavelength regions were 610 to 650 nm and 500 to 540 nm for green and red food coloring, respectively. The DC offset was determined in the 710 to 750 nm range. For the bovine blood, the integrated absorbing wavelengths of interest from 500 to 625 nm were subtracted by the integrated intensity in the 625-750 nm region. Calculating the differences in integrated intensities of certain spectral regions allowed us to quantify spectroscopic alterations in the multi-layer phantoms.

3. Results and discussion

3.1 Depth penetration

Penetration depth of elliptically polarized light was analyzed as a function of optical thickness - $\tau = (\mu_a + \mu_s)D$ where D is the physical thickness of the scattering phantom (Fig. 3). Integrated intensities for all polarization gated scattering signals follow the same general trend (Fig. 3(b)): after an initial increase with an increase in the phantom thickness they reach a plateau. The signal saturation indicates that scattering from the deeper regions in the phantom does not contribute to polarization gated signals as light polarization becomes randomized due to multiple scattering events. The maximum penetration depth for each polarization can be estimated by finding the thickness that corresponds to 90% of the signal at the plateau. Thus, for the parallel polarization, the penetration depth is $\tau \sim 3.13$ that agrees well with previous studies [17, 48]. Penetration depths increase from approximately 5.42 to 32.5 optical thicknesses for elliptical polarizations ranging from 5° to 35° . In contrast, co-polarized signals that are not polarization gated do not reach a plateau for the investigated thicknesses indicating that multiple-scattered photons from deeper regions continue to contribute to the detected scattering (Fig. 3(d)).

It is interesting to note that for each optical thickness up to approximately $\tau \sim 20$, the overall signal intensity decreases from linear to more elliptically polarized light (Fig. 3(c)). This trend can be explained by the fact that light penetration increases with ellipticity. Therefore, as light ellipticity increases more photons are forward scattered and penetrate through scattering phantoms with thicknesses less than $\tau \sim 20$ into the underlying transparent layer and, therefore, do not contribute to the detected backscattered signal. However, at the optical thickness of $\tau \sim 20$, this trend is reversed for light ellipticities ranging from 30° to 45° (circular) as photons that were travelling through phantoms with thicknesses $\tau \leq 20$ are redirected towards the detector at $\tau \geq 20$.

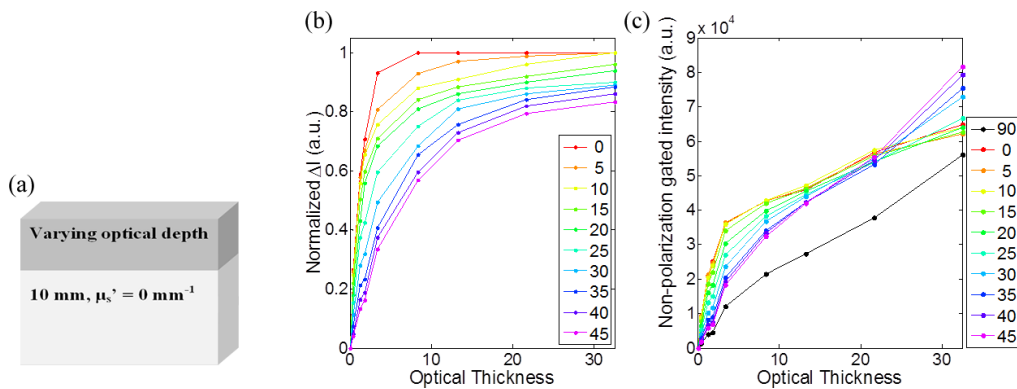


Fig. 3. (a) A schematic of a PDMS phantom used to examine polarized light penetration as a function of depth. (b) Polarization gated, ΔI , and (c) non-gated signals as a function of optical thickness. The polarization gated signals were normalized by the overall maximum integrated intensity that corresponded to the intensity of linear polarized light.

3.2 Depth-resolved spectroscopy

Next, we analyzed the ability of EPRS to detect spectroscopic alterations within a tissue-mimicking phantom. In the first set of experiments, a scattering layer with embedded green food coloring was located at various depths within a three-layer phantom as shown in Fig. 4. Representative polarization gated spectra for the 1700 μm top layer thickness demonstrate spectral changes associated with changes in depth penetration of elliptically polarized light (Fig. 4(b)). Linear polarized light does not exhibit any absorbance associated with the dye as it only interrogates superficially into the top layer of the multilayer phantom. The absorbance from the green food coloring layer gradually increases with an increase in light ellipticity (Fig. 4(a)). Normalized to one elliptically polarized EPRS spectrum (30°) was compared with the absorbance spectrum of the green dye (Fig. 2) using least-squares fitting method to demonstrate that the observed peak in the EPRS spectrum is associated with the absorbance peak of the green food coloring (Fig. 4(b)). The peak positions were 631 and 630 nm and the full width at half maxima (FWHM) – 89 and 60 nm for the EPRS and solution spectra, respectively. This comparison shows a good correlation between the two spectra with the expected spectral broadening in the EPRS measurements due to previously described scattering effects [2, 49]. To analyze these spectral changes for various thicknesses of the top colorless scattering layer we plotted integrated intensities over the wavelength region associated with the green food coloring absorbance (610–650 nm) as a function of light ellipticity in Fig. 4(c)–4(h). These curves have two characteristic regions – a nearly flat parallel to the x-axis line at lower ellipticities of light and a monotonically increasing region at higher ellipticity values. The corresponding polarization gated spectra show that the low intensity flat regions correspond to photons which do not reach the middle colored layer as evident by the lack of the green dye absorbance in the spectra while the regions with monotonically increasing absorbance indicate interrogation of the middle layer (see an example in Fig. 4(b)). As the thickness of the top colorless layer increases, larger values of light ellipticity are required to interrogate the middle layer containing the dye.

The data in Fig. 4(c)–4(h), were used to determine the penetration depth of polarized photons as a function of their ellipticity. To this end we fitted the flat and the monotonically increasing regions of curves in Fig. 4(b)–4(g), to two linear fits. The point of intersect of the two linear fits was used as an estimate of the minimum light ellipticity value that is required to start interrogating the middle colored layer for each top layer thickness. A plot of these ellipticity values as a function of the top layer thickness – the depth to the target - shows a linear relationship between a light ellipticity and a penetration depth (Fig. 4(i)). According to this fit the linear relationship between optical thickness (τ) and light ellipticity is described by

$y = 1.29x + 2.86$ and, therefore, the predicted interrogation depth of the linear polarized light is $\tau = 2.86$ that correlates well with the data shown in Fig. 3 where the interrogation depth for the linearly polarized signal was determined to be $\tau \sim 3$. Linear relationships between probing depth and ellipticity were also observed in imaging experiments performed by Da Silva et al. [37] and in results obtained in single wavelength Monte Carlo simulations by Rehn et al. [23]. However, our results demonstrate that alterations in spectroscopic features can be extracted by tuning the ellipticity in EPRS in highly scattering media.

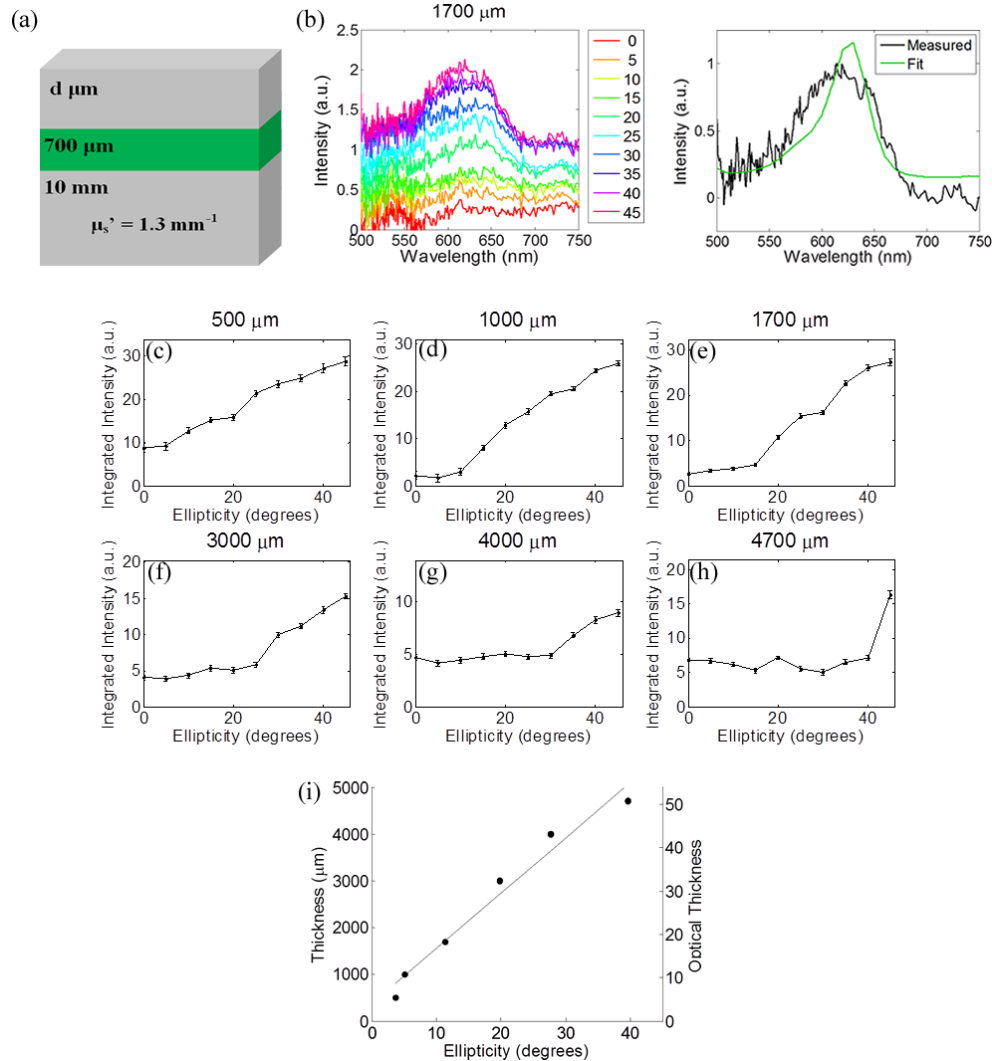


Fig. 4. (a) Multilayer phantom design to evaluate depth-resolved spectroscopy by EPRS where d is the thickness of the top layer. (b) Left: Spectra obtained from the multilayer optical phantom with 1700 μm top layer thickness. Right: comparison of the measured EPRS spectrum with ellipticity of 30° normalized to one and the absorbance spectrum of the green dye. (c-h) Integrated intensities over the wavelengths region associated with the green food coloring absorption (610–650 nm) as a function of light ellipticity for optical phantoms with a top layer thickness of 500, 1000, 1700, 3000, 4000, and 4700 μm . (i) Penetration depths as a function of light polarization; the parameters of the linear fit are $y = 118.62x + 264.07$ ($R^2 = 0.9873$) for the physical thickness (μm) and $y = 1.29x + 2.86$ for the optical thickness.

In the next set of experiments, we evaluated the ability of EPRS to distinguish multiple regions with differing spectroscopic characteristic in a tissue-mimicking phantom. For this

purpose, we constructed a multilayer phantom with two different dyes at different depths as shown in Fig. 5(b). The measured EPRS spectra are presented in Fig. 5(a). Normalized to one circularly polarized EPRS spectrum was fitted to a linear combination of absorbance spectra of the green and the red dyes (Fig. 5(a)). The fit shows that spectral features of the EPRS spectrum are associated with the two dyes. With a 700 μm thick top scattering layer, the signal from the first colored layer with green food dye is monotonically increasing starting at approximately 10° light ellipticity (Fig. 5(c)). The absorbance of the second colored layer with embedded red food coloring dye is not observed until light ellipticity encompasses 20° value (Fig. 5(c)). These data demonstrate that EPRS can be used to detect depth-resolved spectroscopic changes.

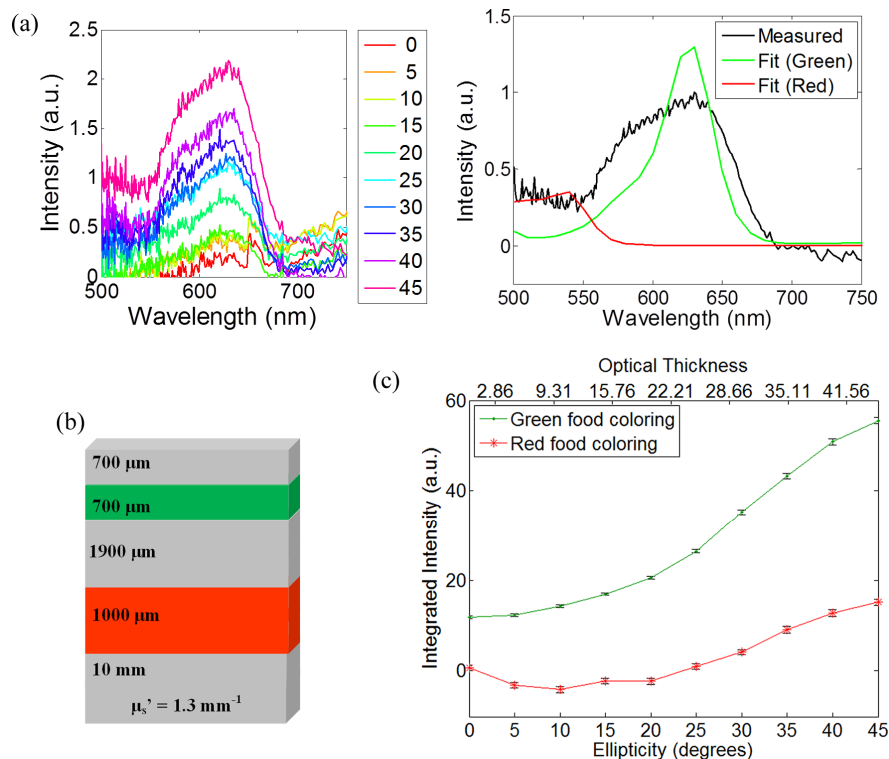


Fig. 5. (a) Left: Measured polarization gated spectra. Right: the least squares fit of the normalized to one EPRS spectrum with ellipticity of 45° using absorbance spectra of the green and the red dyes. (b) Multilayer phantom design with green and red food coloring dyes. (c) integrated intensities over the wavelengths associated with green food coloring (610-650 nm) and red food coloring (500-540 nm) absorption, respectively, as a function of light ellipticity; note, that the absorption of the dyes are corrected by subtracting a DC offset in the 700-750 nm region as described in the Method section.

However, we also noted that signals from the dye layers continue to increase with increase in light ellipticity in experiments shown in Fig. 4 and Fig. 5. This observation posed a question: why does not the absorption signal saturate after penetration depth of a polarized light encompasses thickness of a colored layer; indeed, after this point there is no more dye to contribute to the signal? To address this question, we examined EPRS from a 1700 μm PDMS phantom simulating breast tissue scattering with embedded green food coloring placed on top of two different bottom layers without a dye: one with matching scattering properties and the other one transparent (Fig. 6). EPRS measurements showed that the dye absorption signal is approximately constant for all polarizations for the phantom with the clear bottom layer while it is monotonically increasing with an increase in light ellipticity in the case of the scattering

underlying medium (Fig. 6(a)-6(c)). These results indicate that the illumination light that is backscattered from the turbid bottom layer interacts with dye molecules in the top layer as it travels back to the surface of the phantom. The portion of this backscattered light that preserves its original polarization state contributes to the overall polarization gated signal. As light ellipticity increases, the polarization state is maintained at greater optical thickness and, therefore, more polarization-maintaining photons contribute to the detected absorption signal. This behavior points toward an inherent limitation of EPRS as a depth-resolved spectroscopic modality for detection of various absorbing layers in a turbid media. Indeed, our data in Fig. 4 and Fig. 5 demonstrate that an onset of a spectroscopic area of interest can be detected by EPRS in a depth-resolved manner, however, EPRS cannot accurately identify where an absorbing region ends in a scattering media. This limitation could be compared to shadow artifacts in optical coherence tomography wherein OCT signals beneath areas with a high absorption are significantly decreased that limits imaging of deeper anatomical features [50]. In the case of the transparent bottom layer, the absorption signal is the same for all ellipticity values because the optical thickness of the top layer is approximately $\tau \sim 18.5$ that is very close to the point at which backscattered signal is the same for all ellipticities in our set-up as can be seen in Fig. 3(c).

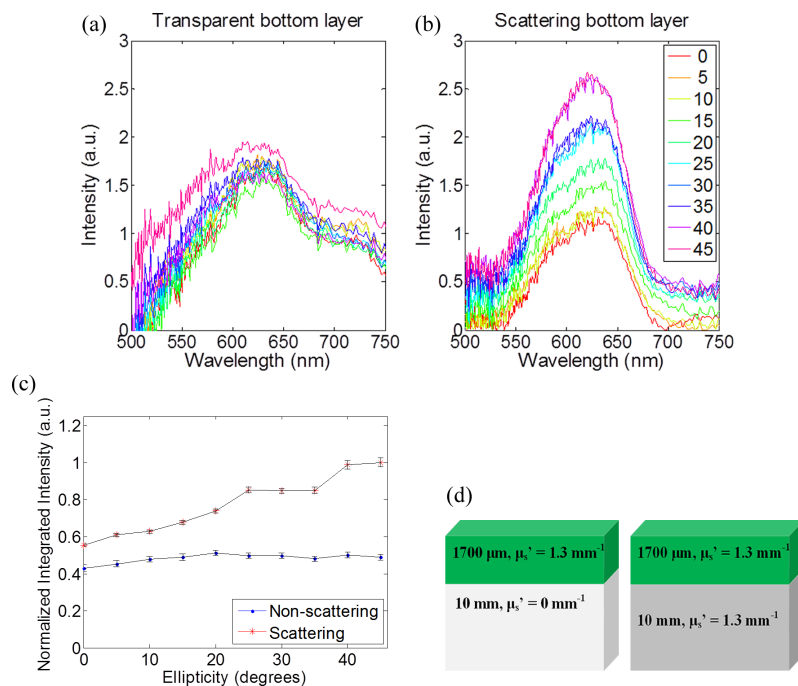


Fig. 6. Spectra of a 1700 μm thick scattering phantom with green food coloring on top of a (a) transparent and (b) scattering bottom layer. (c) Integrated intensities over the 610-650 nm wavelength region as a function of light ellipticity for the spectra in (a) and (b). Schematics of phantom designs is shown in (d).

To demonstrate the feasibility of EPRS with biological absorbers, we carried out experiments with bovine blood in a small capillary (Fig. 7). The capillary was placed at a depth of approximately 2 mm inside a breast tissue mimicking phantom as shown in Fig. 7(c). Spectroscopic features associated with blood absorption were evident in the polarization gated spectra as shown in Fig. 7(a). Two major peaks that can be discerned in EPRS spectra at approximately 542 and 573 nm correlate well with major peaks in the absorbance spectrum of the bovine blood at 540 and 576 nm (Fig. 2(b)). Evidently, EPRS was able to extract spectroscopic features associated with the biological absorber. The signal associated with

blood absorbance was observed starting from an ellipticity of approximately 15° (Fig. 7(a) and 7(b)). This result is in a very good agreement with the depth-penetration vs. ellipticity curve in Fig. 4 which predicts that an absorbing layer at *ca.* 2 mm depth is detectable by light with ellipticities higher than *ca.* 15° . The signal from blood is increasing with an increase in light ellipticity due to the scattering effect that is discussed above.

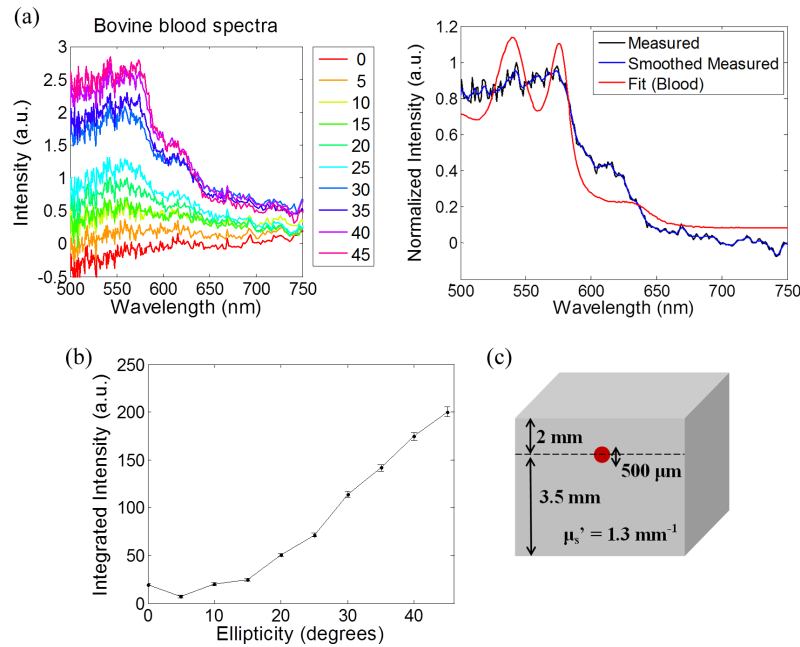


Fig. 7. (a) Left: Polarization gated spectra. Right: comparison of the measured EPRS spectrum with ellipticity of 45° normalized to one and the absorbance spectrum of the bovine blood; the least squares method was used to fit the bovine blood spectrum to the EPRS spectrum. (c) integrated intensities of the spectra in (b) over wavelengths 500 to 625 nm subtracted by the background at 625-750 nm. (c) Schematic of a tissue scattering phantom with a blood filled microchannel.

Next, we evaluated the ability of EPRS to discern spectroscopic areas of interest in biological tissue *in situ* by collecting spectra from microvessels in an ear of a nude mouse (*left* Fig. 8(a)). There are two clearly visible blood microvessels in a region of interest shown in the unpolarized microscope image (*right* Fig. 8(a)). As expected, polarization gated images show a decrease in surface reflections as the interrogation depth increases with light ellipticity (Fig. 8(b)). The apparent decrease in intensity as ellipticity increases from linear to circular polarization is likely due to the thin thickness of the mouse ear. As multiple scattered photons propagate deeper into tissue, they traveled through the ear into the underlying transparent PDMS layer and thus do not contribute to the overall detected signal. This trend is especially evident for the perpendicular image wherein multiple scattered photons comprise the cross-linear image. The blood vessels can be clearly seen in all polarization gated images that indicates their superficial localization. EPRS spectra were collected along the imaging line depicted in Fig. 8(a). Five key areas for depth-resolved spectral analyses were selected and were labeled: *Vessel 1* and *Vessel 2* – two areas with *ca.* 125 μm microvessels, and *Top*, *Middle*, and *Bottom* – the areas without any clearly visible blood vessels, although, the *Middle* region has a very small *ca.* 56 μm vessel (Fig. 8(a)). Relatively strong dips at 560 nm associated with deoxyhemoglobin absorbance are clearly seen at all light ellipticity values for the EPRS measurements of *Vessel 1* and *Vessel 2* regions (Fig. 8(c)). In contrast, *Top* and *Bottom* spectra did not produce prominent dips at 560 nm associated with deoxyhemoglobin absorbance while there is some absorbance from deoxyhemoglobin at low ellipticity values in

the *Middle* region. To determine how blood absorbance measurements with EPRS depend on light ellipticity, we carried out a simple analysis where integrated intensity differences of the polarization gated EPRS spectra - 600 nm – 640 nm background signal minus 530 nm – 570 nm blood absorbing region - were plotted as a function of light ellipticity (Fig. 8(d)). As expected, the *Top* and the *Bottom* areas are characterized by the integrated intensity difference that is close to zero while the signal intensity for *Vessels 1* and *2* regions are relatively large due to the high hemoglobin absorbance. The integrated intensity differences for the *Middle* region with the smaller microvessel fell between the areas with and without microvessels. The signal from the blood vessels decreases with an increase in ellipticity values that can be attributed to a signal attenuation as well as to an overall decrease in the amount of backscattered elliptically polarized photons which propagate through the thin mouse ear.

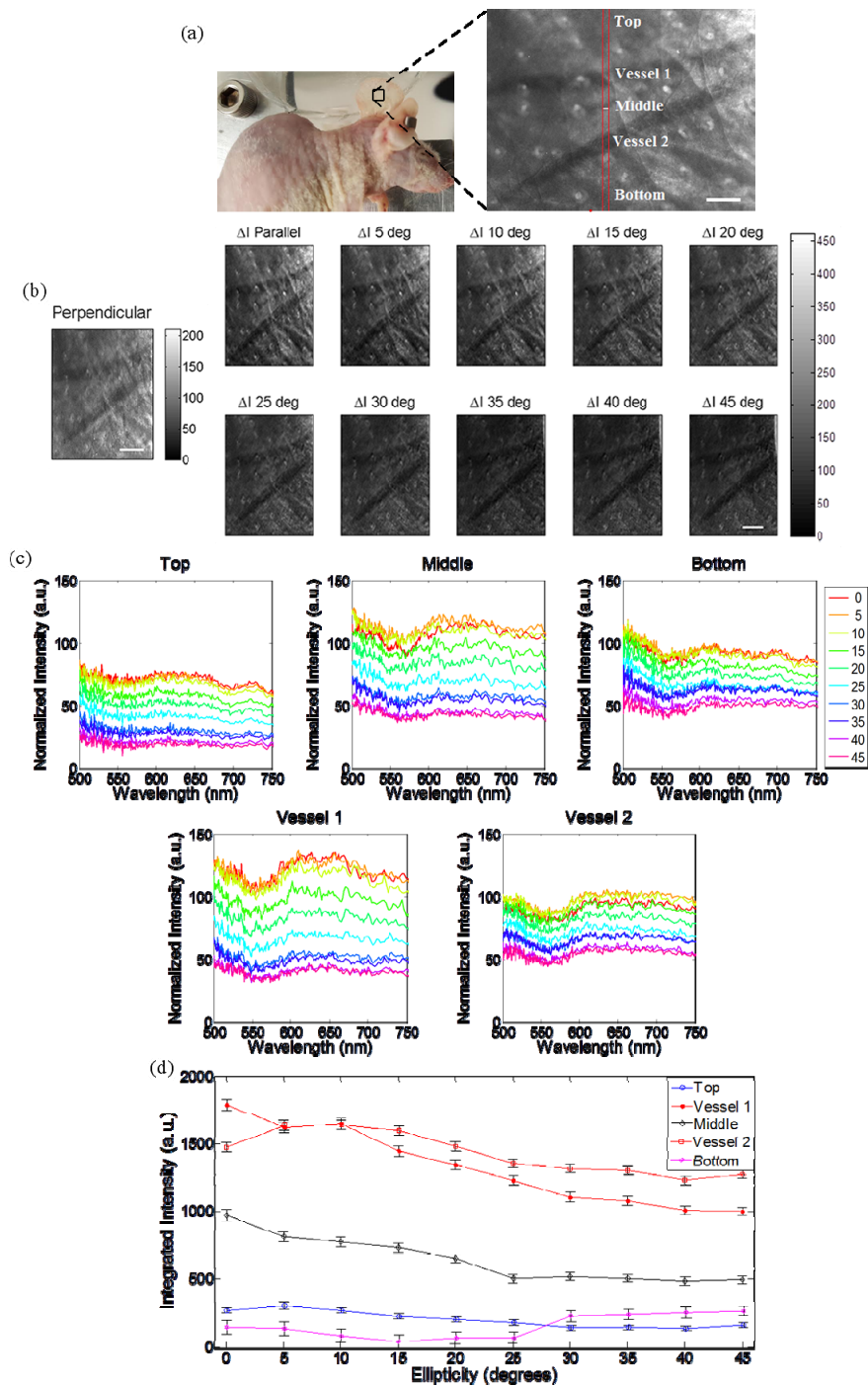


Fig. 8. (a) Left: an image of a nude mouse cadaver with the ear spread on PDMS. Right: Image of a mouse ear with red lines outlining the area that was analyzed by EPRS. (b) Images acquired using perpendicular polarization (left) and co-polarized polarization gated images (right). (c) Polarization gated EPRS spectra of the five areas shown in (a). (d) Integrated intensity differences (600-640 nm background region subtracted by 530-570 nm blood absorbance region) of the spectra shown in (c). Scale bars are 250 μm .

Finally, we demonstrated the feasibility of EPRS as a depth-resolved spectroscopic imaging modality (Fig. 9). To this end, the contrast associated with blood absorbance in EPRS spectra was plotted as a two-dimensional image along the imaging line shown in red in Fig. 8(a). Position of each pixel in the pseudo-colored image in Fig. 9 is defined by the spatial x-coordinate along the imaging slit (20 adjacent imaging pixels were integrated to obtain one pixel in the spectroscopic image in order to improve signal-to-noise ratio) of the hyperspectral PARISS system and by 5° increments of light ellipticity in the z-direction. The light ellipticity was also converted to optical thickness using the linear relationship shown in Fig. 4(i). The image contrast in each pixel was determined by the integrated intensity differences (600 – 640 nm background signal subtracted by the 530 – 570 nm blood absorbance region) of the corresponding EPRS spectra. For example, values for pixels with z-coordinate of 10° ellipticity that corresponds approximately to the optical depth of $\tau \sim 15$ were calculated using EPRS spectra obtained with co-elliptical light at 10 degrees. Together these data generate a two-dimensional depth-resolved pseudo-colored image of blood absorbance. It is important to note that the superficially located blood vessels in this image create “shadows” due to the tissue scattering effect that was described above (see data in Fig. 6).

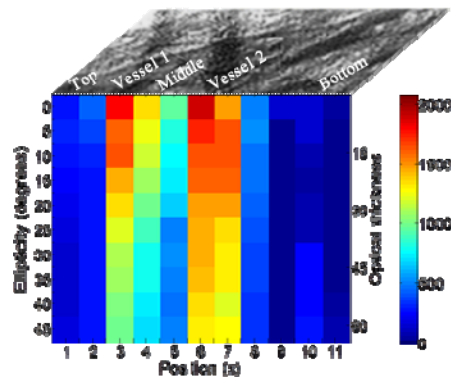


Fig. 9. Two dimensional depth-resolved pseudo-colored EPRS image of blood absorbance in a mouse ear. The image contrast is determined by the integrated intensity differences (600 – 640 nm background signal subtracted by the 530 – 570 nm blood absorbance region). The depth is derived from the fit in Fig. 4. Each spectroscopic pixel in x-coordinate of the image corresponds to 20 integrated imaging pixels along the imaging line of the hyperspectral PARISS system.

4. Conclusion

Here, we report analyses of depth-resolved spectroscopy in a turbid media using elliptically polarized light. Experiments were conducted on tissue mimicking phantoms with embedded absorbers to allow quantitative evaluation of the proposed approach. EPRS was able to detect different spectroscopic signatures in multi-layer scattering tissue phantoms and in biological tissue in situ. It was demonstrated that there is a linear relationship between light penetration depth and ellipticity. The derived relationship between optical depth and ellipticity can be used to probe target depths in future experiments for samples with known optical properties. We showed that this property can be used in development of novel depth-resolved spectroscopic imaging approaches in biological tissue. Potential implementations can evolve using a line imaging as demonstrated in this study or can be based on a single scanning imaging optical fiber previously reported in [51, 52].

Acknowledgments

This work was supported by NIH grant R01 CA103830 BRP. Maria Bailey was also supported by the NIH T32 training grant (EB007507).